Type II superlattice detectors at SCD

P.C. Klipstein, Y. Benny, Y. Cohen, N. Fraenkel, R. Fraenkel, S. Gliksman, A. Glozman, I. Hirsh, O. Klin, L. Langof, I. Lukomsky, I. Marderfeld, B. Milgrom, H. Nahor, M. Nitzani, D. Rakhmilevich, L. Shkedy, N. Snapi, I. Strichman, E. Weiss and N. Yaron.

.

SemiConductor Devices P.O. Box 2250, Haifa 31021, Israel

ABSTRACT

The InAs/InSb/GaSb/AlSb family of III-V alloys and superlattice materials offer unique possibilities for band structure engineering, because they can be grown on GaSb or InSb substrates with high quality and satisfactory control of strain, doping and composition. The band profiles and oscillator strengths are also quite predictable, enabling full simulation of detector performance from a basic knowledge of layer and stack thicknesses. In conventional III-V *p*-*n* devices, Shockley-Read-Hall (SRH) traps generate a significant flow of thermal carriers in the device depletion region. At SCD, we have overcome this problem by developing XB*n* and XB*p* barrier device architectures that suppress these depletion currents, leading to higher operating temperatures or lower dark currents. Our first barrier detector product was launched in 2013 and operates at 150K. It uses a mid-wave infrared (MWIR) XB*n* device with an InAsSb absorber well matched to the most transparent of the atmospheric windows, at wavelengths between 3 and 4.2µm. However to span the full MWIR and to sense the long-wave infrared (LWIR) spectrum, we have investigated InAs/GaSb type II superlattices (T2SLs), because they offer full tunability. In this work we show that minority carriers in *n*-type T2SLs are localized and diffuse by variable range hopping, even when the period is short and the valence mini-band has a width of 30-40 meV. Unfortunately, this leads to sub-micron diffusion lengths and a low quantum efficiency (QE) of ~20% in a full MWIR XB*n* device. On the other hand, *p*-type layers exhibit "metallic" minority carrier transport with much longer diffusion lengths, typically ~7 µm in our LWIR device layers. The successful development of *p*-type devices has led to our second barrier detector product, which uses an XB*p* LWIR T2SL and operates at 77K with a cut-off wavelength of 9.5 µm, a focal plane array (FPA) QE of ~50% and background limited performance up to ~90K at F/3. Moreover, the FPA operability is typically above 99.5%, based on stringent production-line criteria. Together with high spatial uniformity and good temporal stability, these barrier detectors are already a realistic alternative to MCT photodiode arrays, and further products operating at other wavelengths will be launched in due course.

Keywords: Infrared Detector, Focal Plane Array, Type II superlattice, XB*n*, XB*p*, *p*B*p*, MWIR, LWIR.

1. INTRODUCTION

Over the last decade there has been a steadily increasing interest in the development of the InAs/InSb/GaSb/AlSb family of III-V alloys and superlattices as an alternative to HgCdTe alloys for the fabrication of infrared detectors. While HgCdTe is very attractive for its high degree of band gap tunability and its potential for very low dark currents, it requires specialized CdZnTe substrates for the highest quality growth and can suffer from limited uniformity and

stability. For this reason, InSb is still the champion for large format photodiode arrays[1], and customers are prepared to accept operating temperatures at or even below 100 K[2] in a full mid wave infrared (MWIR) InSb focal plane array (FPA), because of its excellent uniformity and stability. Although high quality HgCdTe operating according to Rule 07[3], can in principle offer the same dark currents at higher temperatures, ~140K for *p*-on-*n* and ~120K for *n*-on-*p*[4], good spatial uniformity and high temporal stability at the focal plane array (FPA) level often dictate lower operating temperatures. More recently even higher operating temperatures have been announced in Rule 19, for fully depleted HgCdTe photodiodes[5]. The growth and processing of these devices is even more challenging, and it remains to be seen if such devices will lead to a significant increase in performance of the next generation of HgCdTe based FPAs.

Today SCD is one of the largest manufacturers of InSb FPAs, in formats up to 3 megapixels and pitches down to 10 µm. The continuing success of InSb detector arrays has lead SCD to adopt a strategy based mainly on III-V materials, building on the good availability of high quality commercial substrates, and the potential for ease of manufacturing and greater yields. To this end, SCD has developed and patented new XB*n* and XB*p* device architectures,[6, 7, 8] which exploit the novel band alignments of lattice matched III-V materials, and reduce the dark currents[9] to levels comparable with Rule 07.

The first barrier detector product family started with Kinglet, a 640 × 512 pixel, 15 µm pitch FPA launched in 2013 and based on a MWIR XB*n* device with an InAsSb absorber[10]. It operates at 150K in the most transparent region of the atmosphere (3 - 4.2 µm) and is ideal for applications in which small size, weight and power (SWaP), a long mean time to failure (MTTF) or extremely long range observation are important. Examples include small payload airborne, 24/7 surveillance, and hand held devices.

To span the full MWIR atmospheric window (3 - 5 µm), and to operate in the long-wave infrared (LWIR) window (8 - 14 µm), we have developed an approach based on InAs/GaSb type II superlattices (T2SLs), because they offer the necessary tunability and can be grown in a barrier architecture. In this work we show that full MWIR *n*-type devices with minority holes exhibit low dark currents. Unfortunately, their quantum efficiency (QE) is relatively low because the valence mini-band is not wide enough to delocalize the holes, even in XB*n* devices using T2SLs with a relatively short period. In *p*-type devices with minority electrons, however, the electrons exhibit "metallic transport" with much longer diffusion lengths and therefore a much higher QE. Work on these devices has led to our second barrier detector product family which entered the market in 2016. It uses an XB*p* LWIR T2SL and operates at 77 K with a cut-off wavelength of 9.5 µm and an FPA pixel operability above 99.5%. The FPA has a QE of ~50% with background limited performance up to ~90K at F/3.

In the development of our present and future barrier detector product lines, simulation tools in which the band profiles and optical transition strengths can be predicted accurately, are playing an extremely important role. These tools are based on a form of the **k · p** model adapted to narrow gap systems were interface contributions are explicitly included[11], and also on optical transfer matrix modelling combined with diffusion theory[12, 13]. These tools enable full

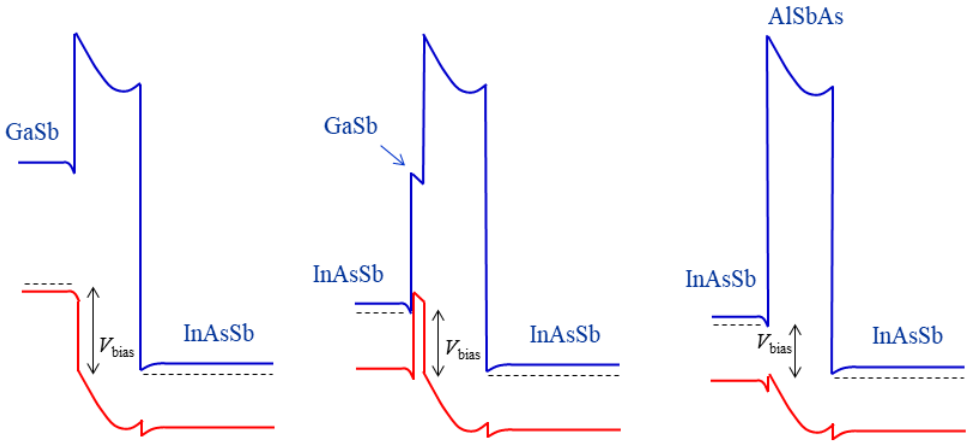

Figure 1:
XBn barrier detectors according to US patents: US 7,795,640, US 9,627,563 and US 8,004,012, respectively, in which the BL and AL are both *n*-type and form the same identical unit in all three cases, while the CL is different. In the middle diagram, an intermediate layer is added between the CL and BL to promote the efficient trapping of minority carriers and their transfer to the CL.

simulation of detector performance from a basic knowledge of layer and stack thicknesses. The combination of relatively simple measurements on test devices as a function of device dimensions and temperature, and device simulations as a function of the diffusion length and minority carrier lifetime, allows us to establish the values of these key parameters and provide an insight into what can limit device performance.

After a brief introduction to barrier devices, this paper first discusses the criteria for metallic conduction of minority carriers and our heretofore failed attempts to achieve it in XB*n* T2SL devices, both with or without gallium. This provides the background for our development of InAs/GaSb XB*p* devices, which are described in the next section. In this case, their very much higher minority carrier mobility provides a clear demonstration of metallic conduction. Nevertheless, the minority carrier lifetime is shown to be very small in all InAs/GaSb T2SL devices, consistent with reports of other workers, and is likewise attributed to strong Shockley-Read-Hall (SRH) recombination. Possible scenarios are discussed in the following section, which might lead to such strong SRH recombination and the absence of Auger recombination, even in cases where Auger might be expected to play a significant role. The implications of our findings are summarized in the final section, where possible pathways for further device optimization are discussed.

2. BARRIER DETECTORS BASED ON BULK InAsSb

In 2003, SCD patented its first barrier detector, whose band profile at operating bias is depicted in the left hand panel of Figure 1. This device is grown on a GaSb substrate with a *p*-type GaSb contact layer (CL), an n-type barrier layer (BL) and an InAsSb active layer (AL), which absorbs the radiation incident on the detector from the right hand side with wavelengths shorter than 4.2 µm. In subsequent variations, the contact layer was changed to *n*-type InAsSb (right hand panel), or a combination of GaSb and n-InAsSb (middle panel). These changes lead to a lower operating bias, and more efficient transfer of minority carriers into the CL, respectively. The most important features, however, in common with all three designs are (i) the unipolar n-type doping of the AL and BL, which avoids any depletion in the narrow band gap AL and (ii) the blocking of majority carriers by the BL which also allows the free passage of minority carriers. These two features allow the efficient collection of photo-generated carriers, which diffuse freely into the CL, and the suppression of Generation-Recombination (G-R) dark current which only occurs in the fully depleted wide band gap BL. As a result, the dark current is close to the theoretical narrow gap diffusion limit, and high operating temperatures at or in excess of 150K can be achieved, together with quantum efficiencies above 70%. This technology is very robust and produces excellent images with a very high pixel operability, as shown for 15 and 10 µm pitches in the examples presented in Figure 2.

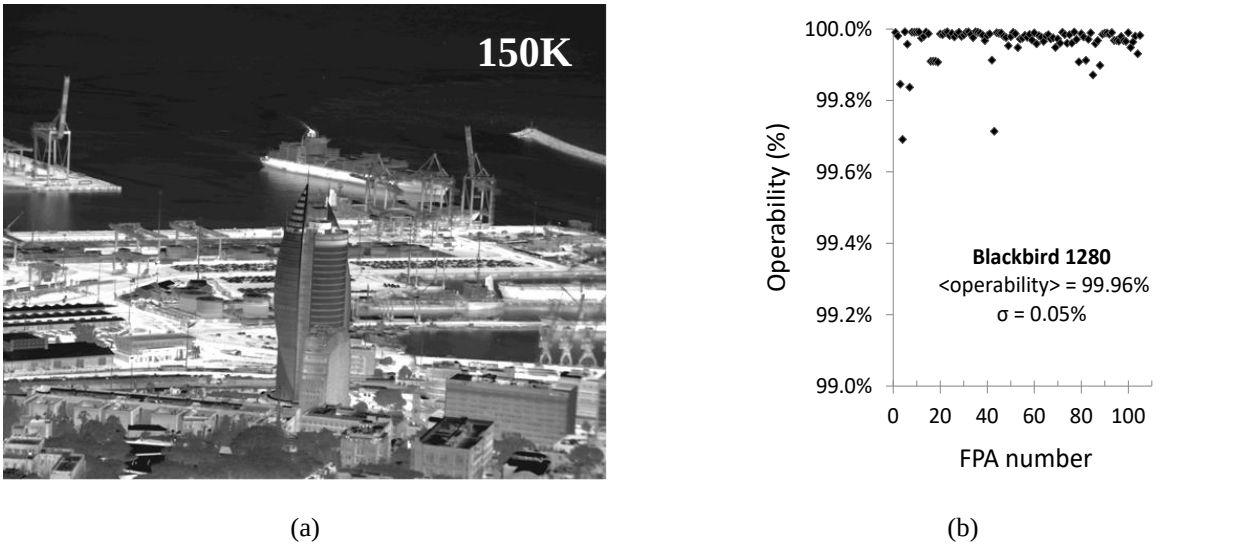

(a) (b)

Figure 2:
(a) Image from 1 Megapixel Hercules detector with 15µm pitch, registered at 150 K and (b) pixel operability according to strict production line criteria for a recent batch of 1 Mega-pixel Blackbird detectors with a pitch of 10 µm.

3. TYPE II SUPERLATTCE BARRIER DETECTORS

3.1. XB*n* detectors

As mentioned in the Introduction, the devices based on InAsSb described in the previous section have a cut-off wavelength of 4.2µm which is very well matched to the most transparent of all the infrared atmospheric windows. However, if other cut-off wavelengths are required to span other atmospheric windows in the MWIR or LWIR wavelength regions, a material is required whose composition or structure can be tuned to give the desired performance. We have chosen to investigate InAs/GaSb T2SLs because they exhibit stronger absorption than gallium free InAs/InAsSb T2SLs, particularly in the LWIR wavelength region, and offer greater flexibility in terms of their mini-band properties.

An *n*B*n* structure like that shown in Figure 3(a) is attractive because it can be grown with a tall barrier that is closely related to the barrier material used in the InAsSb XB*n* structures described in the previous section. Therefore, a similar passivation treatment can be applied after mesa delineation, and it indeed appears to work quite well. The drawback however, is the narrow width, B_H, of the hole mini-band. Efficient "metallic" transport of the minority holes across the AL requires a low effective mass, which is related to the mini-band width by the simple formula: $m^*_H = \hbar^2 / 2B_H e d^2$ where d is the T2SL period. By choosing a short period of d = 9 monolayers (ML) in a full MWIR T2SL with a cut-off wavelength of 5µm, a zone centre mini-band width of 33meV has been calculated using the **k** · **p** model described in the Introduction. This yields a fairly low hole mass of m^*_H ~0.017 m_0, where m_0 is the mass of the free electron. However, another important factor is the variation of the hole confinement energy with disorder, in particular fluctuations in the GaSb quantum well width. The mini-band is formed by the overlap of wave functions from each well, and if the confinement energy fluctuations, ΔE_H, are greater

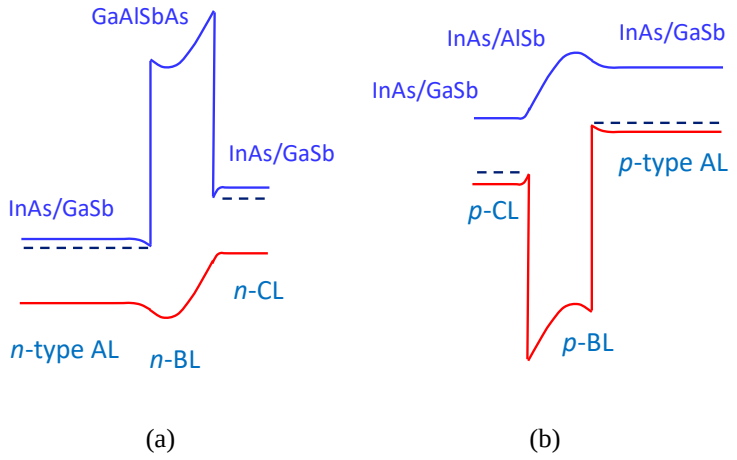

Figure 3:
Band profiles at operating bias of *n*B*n* and *p*B*p* devices with an InAs/GaSb T2SL AL, in which the BL is intentionally doped with the same type as the AL (US patent 8,014, 012)

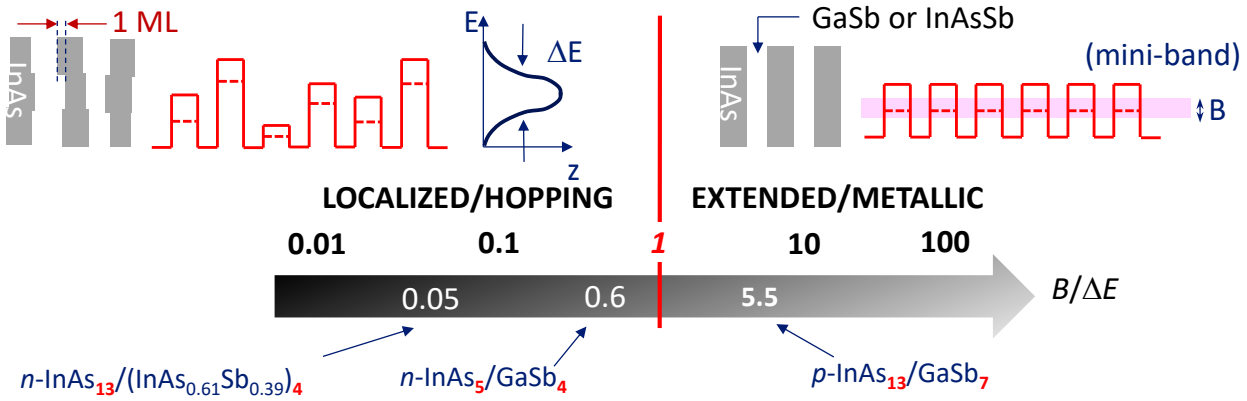

Figure 4:
The metal-insulator transition and its relation to the energy fluctuation, Δ*E*, caused by e.g. well width variations (top left) and the mini-band width, *B* (top right). Values of the *B*/Δ*E* ratio of the minority carriers, calculated from the **k** · **p** model assuming a ±1 ML layer width variation, are shown on the grey arrow for two *n*-type full MWIR T2SLs, and a *p*-type LWIR T2SL

than the mini-band width in the perfectly ordered T2SL, then localized states will be formed and hopping conduction will occur, first by excitation to the "mobility edge", and at lower temperatures by direct variable range hopping between them, instead of by mini-band metallic transport[14]. A metal-insulator transition is expected to occur roughly when $B_H/\Delta E_H = 1$.[14] In the present case we have estimated ΔE_H , using the **k · p** model, by shifting the InAs/GaSb interface by one monolayer without changing the T2SL period and calculating the change in energy of the valence mini-band edge. We find that $B_H/\Delta E_H \sim 0.6$ for the short period T2SL. As depicted in Figure **4**, this is fairly close to the value expected for a metal - insulator transition, so metallic conduction might still occur if well - width fluctuations are the dominant source of disorder, but are not too large. *n*B*n* devices were therefore investigated with two different AL thickness, L_{AL}, of 1.5 and 2.6 µm. QE was measured as a function of bias in the wavelength range $3.2 \leq \lambda \leq 3.6$ µm on 150 × 150 µm^2 devices at 110K, and the results are shown in Figure 5 (a). For both devices, the QE shows an initial rapid increase with bias up to a shoulder, followed by a slower rise thereafter. The initial rise is related to the reduction of the electrostatic barrier (EB) depicted by the hump in the valence band of the BL in Figure 3 (a). The EB prevents the flow of minority holes created by photo-absorption, and only vanishes at the shoulder bias. Beyond this bias the holes can flow freely to the CL, but the AL begins to deplete. The continuing rise in QE is consistent with a short diffusion length, since the increasing depletion width of the AL with bias contributes an increasingly significant proportion of the photo-carrier collection volume. As described in the Introduction, we are able to simulate the QE by calculating the absorption coefficient with our **k · p** model, using this as an input for an optical transfer matrix calculation which is combined with a diffusion model.[12,13] In the present case we find that diffusion lengths of 0.65 and 0.8µm, reproduce the observed QE values at λ=3.4µm, depicted by the dots at the device operating bias values (just beyond the shoulder bias) of the thin and thick AL devices, respectively, in Figure 5 (a). The short diffusion lengths also explain why the thicker sample has a lower QE value because a significant proportion of the radiation is absorbed too far away from the BL for the photo-carriers that it creates to reach the BL before they recombine.

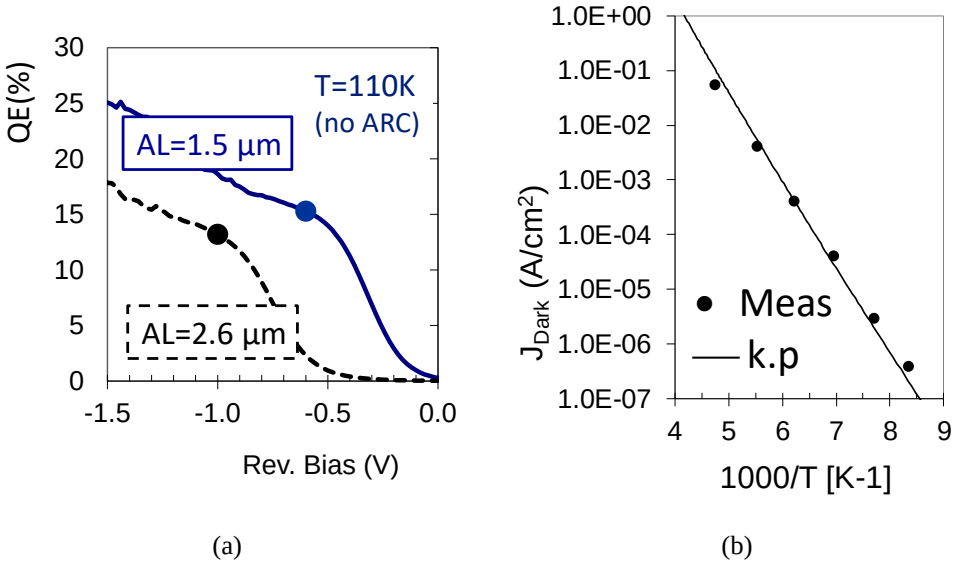

(a) (b)

Figure 5:
(a) Bias dependence of QE at 110K in the wavelength range $3.2 \leq \lambda \leq 3.6$ µm, for *n*B*n* devices with no anti-reflection coating and a short period T2SL AL of thickness 1.5 µm (solid line) and 2.6 µm (broken line), respectively. (b) Temperature dependence of the dark current density measured on the device with the thicker AL (points) and fit to **k · p** model, as described in the text.

In Figure 5 (b), the points show the logarithm of the dark current of the thick AL sample measured in a device with a mesa size of 300 × 300 µm^2, plotted as a function of the reciprocal temperature. The solid line shows a fit to the diffusion current formula: $J_{diff} = ep_{n0}L_{D\perp}/\tau_{min}$ where τ_{min} is the minority carrier lifetime, $L_{D\perp}$ = 0.8 µm is the vertical diffusion length, and $p_{no} = n_i^2/N_D$ is the minority carrier concentration given in terms of the intrinsic carrier concentration, n_i, and the AL doping, N_D. A doping value of N_D = 4 ×10 ^{15} cm^{-3} was determined by capacitance measurements, [15] while n_i is calculated from the **k · p** model as described in Ref. 13, in this case using a value of 0.255 eV for the zero temperature band gap and Varshni parameters of α = 2.55 ×10^{-4} eV/K and β = 75 K. These were obtained by fitting the observed temperature dependence of the T2SL photoluminescence peak position to the Varshni

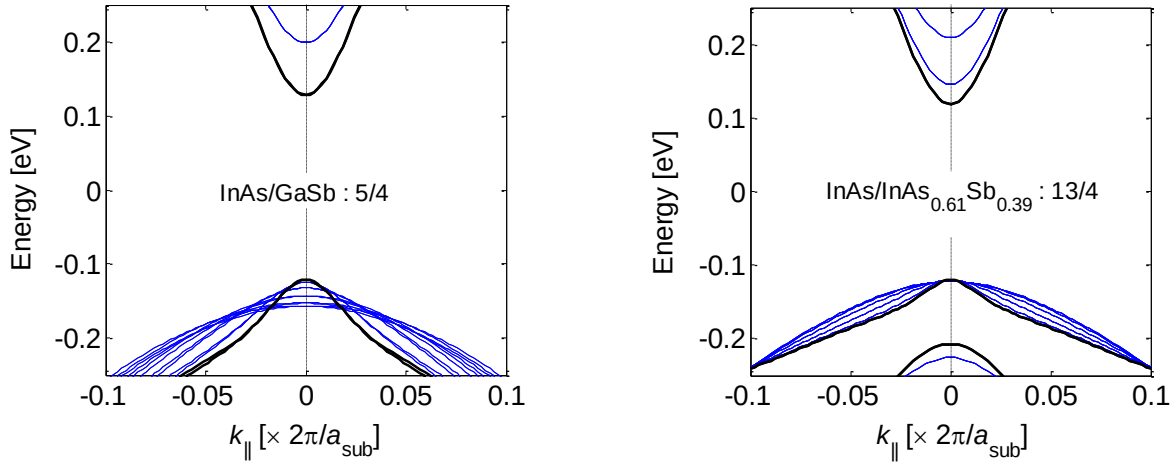

(a) (b)

Figure 6:
In-plane valence band dispersion calculated with the **k · p** model for short period superlattices made from (a) InAs/GaSb and (b) InAs/InAs$_{0.61}$Sb$_{0.39}$, with a cut-off wavelength of 5.0 μm at 77K. In each case, the black curve corresponds to a wave-vector in the growth direction of q_z=0 and the blue curves to ten equally spaced values of q_z up to the mini-zone boundary, π/d. In (b) the energies have been upshifted by 0.25 eV with respect to the energies in (a).

formula[16]. A value of τ_{min} = 22 ns was found to give the best fit of the theoretical diffusion current to the experimental points, which is fairly consistent with direct lifetime determinations by other workers on *n*-type MWIR T2SL samples[17].

The values of the diffusion length and lifetime allow us to calculate the hole mobility from the Einstein relation: $\mu_H = \frac{e}{k_B T} L_{D\perp}^2 / \tau_{min} = 31\ \text{cm}^2/\text{Vs}$. This value is very small, in spite of the relatively low effective mass in the valence mini-band discussed above. From the mobility and the mass value estimated above, a scattering time is found of $\tau_s = \mu_H m_H^* / e = 2.9\ \text{fs}$. Assuming non-localized carriers, the thermal velocity is $v_{thermal} = \sqrt{k_B T / 2\pi m_H^*} = 4\times10^4\ \text{m/s}$. The mean free path is therefore $l = v_{thermal}.\tau_s = 1.2\ \text{Å}$. According to the Mott-Ioffe-Regel (MIR) rule[14, 18], metallic conduction can only occur when $l > d$, where *d* is the lattice period of the material. Since $d \approx 27$ Å in the present T2SL, the MIR condition is clearly not fulfilled. Simply stated, for metallic transport to occur, the wave function has to be coherent over more than a single period of the structure. Since a mean free path cannot be found that is both consistent with the data and with metallic conduction, this provides strong experimental evidence that the holes are localized, and that the transport is by hopping from one localized state to another.

Mott[14] showed that the MIR rule is actually equivalent to the condition for the metal-insulator transition given in Figure 4. This can be demonstrated by the following simple argument for a one dimensional superlattice. For an energy dispersion, $E = -\frac{B}{2}\cos kd$, the maximum carrier velocity is at E = 0 and equal to $v_{max} = \frac{Bd}{2\hbar}$. If the scattering time, τ_s, corresponds to the MIR condition that the mean free path is less than one period, i.e. $v_{max}\tau_s < d$, then this is equivalent to $\frac{\hbar}{\tau_s} > \frac{B}{2}$. According to the Heisenberg uncertainty principle, the left hand side is a measure of the energy distribution due to the disorder, or $\Delta E \geq \frac{\hbar}{\tau_s}$, which is consistent with the condition for an insulator given earlier: $\frac{B}{\Delta E} < 1$.

It is interesting to point out that **k · p** calculations for a short period InAs$_{13}$/(InAs$_{0.61}$Sb$_{0.39}$)$_4$ gallium free T2SL, designed to have the same cut-off wavelength of 5.0 μm at 80K, yield a value of $B_H/\Delta E_H \sim 0.05$ for the hole mini-band at the zone centre. This is more than one order of magnitude smaller than for the InAs/GaSb T2SL and well below the value for a metal-insulator transition discussed above (see Figure **4**). The calculated valence band dispersions, both parallel and perpendicular to the superlattice layer plane, are compared for the two cases in Figure 6, where the much

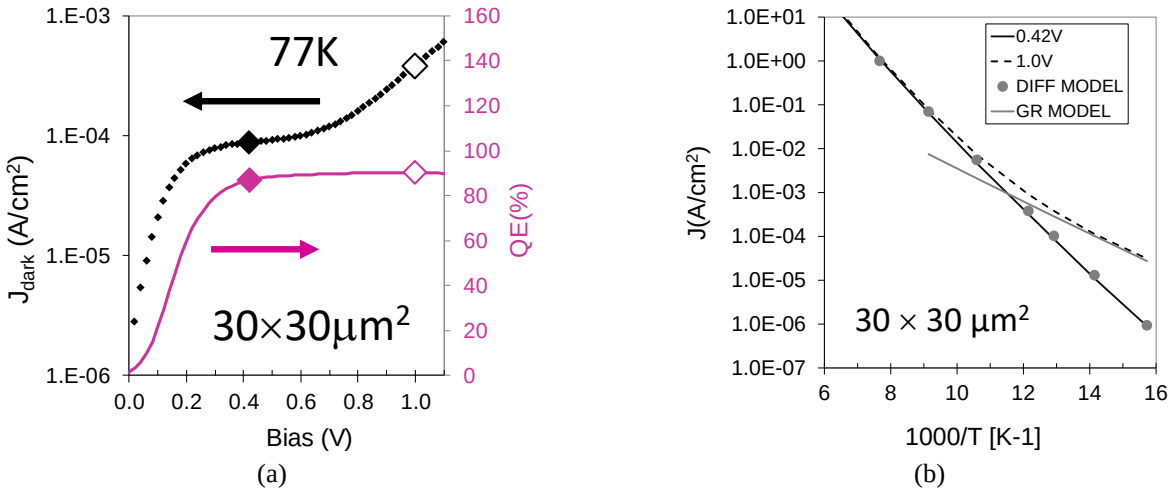

Figure 7:
(a) QE and dark current density at 77 K vs bias, for a 30 × 30 µm^2 test device made from an LWIR XBp wafer with an AL cut-off wavelength of 9.8 µm and (b) temperature dependence of the dark current at a bias of 0.42 V and 1.0V, indicated in (a) by full and open diamonds, respectively, and shown as solid and broken lines. Fits to the diffusion and GR models described in the text are shown in grey as points and a short line, respectively.

narrower mini-band width of the gallium free superlattice is quite evident. Therefore, conduction in the gallium free material should also be by hopping between localized states. This is consistent with the work of Olson et al. on LWIR gallium free T2SL bipolar transistors, who observed a similarly low vertical mobility of 26 cm^2/Vs at 70K, which they associated with hopping transport[19], and with recent theoretical calculations by Bertazzi et al.[20] Soibel et al. also report mobility values below 7.2 cm^2/Vs, in a MWIR *n*B*n* device at temperatures below 150K.[21] The reason that relatively large diffusion lengths are observed in gallium free T2SL devices[21, 22] is related to their long minority carrier lifetime of several microseconds when the AL doping is sufficiently low.[23] In the present case, a lifetime of 1 µs would increase the diffusion length by a factor of $\sqrt{1000 / 22}$, to a value of 5.4 µm which is comparable with the gallium free values.

We finish this section by estimating the potential performance of a full MWIR XB*n* device based on the short period InAs/GaSb T2SL. The results in Figure 5 (a) are measured without an anti-reflection coating (ARC). With an ARC, we can expect a QE of 21% at 110K in the device with a 1.5 µm thick AL. Based on other measurements not included here, we estimate that the QE increases to about 23% at 123K, at which temperature the photo-current at F/3 is about 20 × higher than the dark current shown in Figure 5 (b). Thus, such a full MWIR detector has the potential to exhibit stable background limited performance with an operating temperature in the vicinity of 125 K, albeit, with a relatively low QE of 23%.

3.2. XB*p* detectors

In order to increase the QE in a InAs/GaSb barrier detector, it is necessary to go to an XB*p* design, where the minority carriers are electrons with a lower effective mass, and where the ratio of the electron mini-band width to the band edge fluctuation energy is significantly greater than one. It is shown below that both these conditions are fulfilled.

Some of the initial steps in the development of XB*p* devices have been discussed previously[24]. Figure 7 shows dark current and QE results for a LWIR XB*p* test device with a cut-off wavelength of 9.8 µm, similar to the devices used in our 640 × 512 / 15 µm pitch, Pelican-D LW production FPA. The test device in this case has an area of 30×30 µm^2. The T2SL period is longer than for the MWIR case discussed above, yet the QE is significantly higher. The solid diamonds in Figure 7 (a) are plotted at the detector operating bias of 0.42V, which is just beyond the shoulder in the QE, according to the criterion discussed in the previous section. In contrast to the MWIR *n*B*n* device with a small diffusion length and a QE that increased monotonically with bias, the QE in the XB*p* device saturates beyond the QE shoulder, consistent with a much larger diffusion length. The QE in Figure 7 (a) is calculated by normalizing the

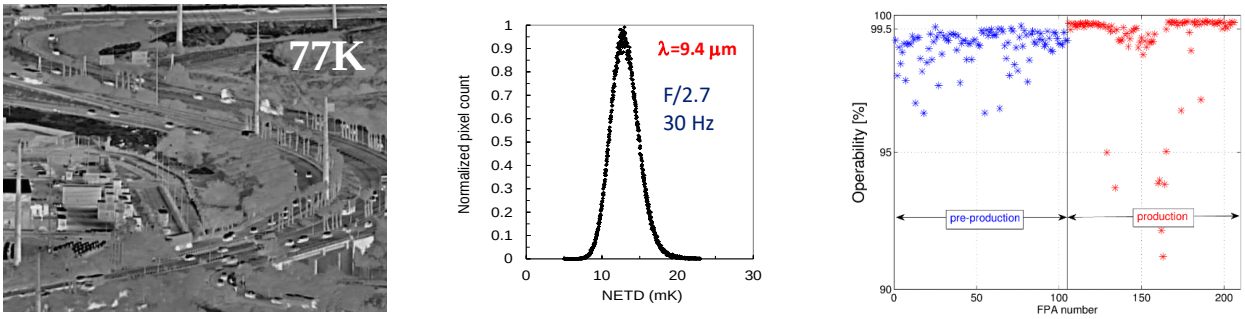

(a) (b) (c)

Figure 8:
Pelican D-LW FPA operating at 77K: (a) Image registered with a with an F/2.7, 60-240 mm focal length zoom lens. The distance of the scene is 9.5 km. (b) NETD distribution for effective frame rate of 30 Hz. (c) Evolution of FPA pixel operability based on strict production line criteria during the initial production phase.

measured photocurrent to the delineated mesa area. Since the diffusion length is large, there is also a significant contribution to the signal from carriers excited beyond the mesa boundaries, that then diffuse inside and are collected. Further data has been reported previously for test devices with different dimensions made from this same XB*p* wafer, where it was shown that the true QE extrapolated to infinite device dimension is 45% with no ARC, and 64% with an ARC. Allowing for the smaller contact-metal fill-factor in an FPA, where a smaller proportion of the radiation is reflected back for a second pass, a QE was estimated of 50%, which agrees quite well with the measured FPA value. These results were fitted previously, as for the *n*B*n* device above, using our **k** · **p** model combined with an optical transfer matrix calculation and diffusion model, to yield a diffusion length in the T2SL growth direction of $L_{D\perp}$ = 6.6 µm[13].

The dark current in Figure 7 (a) exhibits a plateau, with a point of inflection at the operating bias corresponding to the peak dynamic resistance of the device in the plateau region. At higher bias, the current starts to rise more rapidly, increasing above the operating value by a factor of 4.4 at a bias of 1V. This is related to the onset of GR current, which dominates at the higher bias, as demonstrated in Figure 7 (b). In this Figure, the logarithm of the dark current is plotted against the reciprocal of the temperature at the two bias values. At the operating bias a single slope behavior is observed, consistent with a diffusion limited current as shown by the grey points, which follow a variation of the form $T^{2.5}\exp\left(-hc/\lambda_A k_B T\right)$ with λ_A=9.6 µm, while at the higher bias the current deviates from the diffusion line at temperatures below 90K, exhibiting a variation with roughly half the slope in this region, as shown by the grey line, which is proportional to: $T^{1.25}\exp\left(-hc/2\lambda_A k_B T\right)$. The value of λ_A is very close to the low temperature T2SL band gap wavelength of 9.8 µm, measured at 10K by photoluminescence spectroscopy. The temperature exponents have been discussed previously[25], and deviate slightly from the usual values of 3 for diffusion behavior and 1.5 for GR behavior, because of the two dimensional character of the valence band.

Some important aspects of our production Pelican D LW detector are presented briefly in Figure 8. Figure 8 (a) shows an image of traffic at a distance of 9.5 km registered with an F/2.7, 60-240 mm focal length zoom lens. The detector operating temperature is 77 K and the nominal cut-off wavelength is 9.3 µm. The graph in Figure 8 (b) shows the noise equivalent temperature difference (NETD) distribution when the detector is operated at 240Hz with 8 frame averaging, giving an effective frame rate of 30Hz. The NETD distribution is fairly narrow with a peak at 13mK. Figure 8 (c) shows the evolution of the pixel operability in the early stages of our production line. At the end of the preproduction phase, shown in blue, changes were introduced into the molecular beam epitaxy (MBE) process by which the T2SL wafers are grown, which resulted in a dramatic increase in operability. During the first full production phase, shown in red, a misalignment problem with the lithographic mask was discovered that resulted in the operability reduction seen around the 130th-170th FPA. After this had been eliminated, we found that more than 60% of FPAs had an operability above 99.5%.

The dark current in Figure 7 (b) has been fitted to the **k** · **p** model in a similar way to that described in the previous section for the MWIR *n*B*n* device, and as reported in detail in Ref. 26. A lifetime of 7.5 ns was determined, which is reasonably consistent with direct time resolved optical measurements on similar samples reported in the literature[27]. As shown above, a knowledge of the minority carrier lifetime and diffusion length allows us to determine

the electron mobility, and this comes to 8,800 cm^2/Vs at 77K. The electron mini-band is much wider than the hole mini-band discussed above, and has a very small effective mass of 0.022 m_0. The high electron mobility and low mass correspond to a large mean free path of about 100Å, which is greater than the T2SL period, demonstrating clearly that the electron transport is metallic. It contrasts with the low hole mobility and low mean free path in the *n*B*n* case, which was shown above to correspond to localized hopping transport. The ratio of the electron mini-band width, B_E, to the electron energy fluctuation, ΔE_E, is also large: $B_E / \Delta E_E = 5.5$, again consistent with metallic transport as discussed above and shown in Figure **4**. Thus even though the lifetime is very short, the transport is metallic and the diffusion length is reasonably large. We have shown previously[26] that the value of $L_{D\perp}$ = 6.6 µm estimated in this case corresponds to an internal QE of nearly 90%.

The very short lifetime observed here and in general in T2SLs has been related by ourselves and other workers to very strong SRH processes[26, 28]. Although it was originally thought that the T2SL band structure leads to very strong suppression of Auger processes, more recent work has shown that this effect may be less important, except for very long wave length infrared (VLWIR) devices[28]. It was suggested in Ref. 26 that Auger recombination may instead be suppressed in *p*-type T2SLs by donor like SRH traps, which attract electrons when empty, but repel holes, leading to a short minority electron recombination time because of the electrostatic attraction, but weak Auger processes due to poor electron-hole overlap. If some other trap species is also present with acceptor like character, this could account for the short lifetime observed above for the *n*-type T2SL. In this case, a full trap is negative, attracting minority holes and again leading to fast recombination. In both cases, the weakening of Auger processes allows relatively high doping of the photon absorbing layer and a low diffusion limited dark current.

4. CONCLUSIONS

Barrier devices offer the prospect of low dark currents and high operating temperatures in III-V materials. The absorbing layer can either be a bulk material, such as InAsSb used in our MWIR XB*n* line of detectors operating at 150 K with a 4.2 µm cut-off, or a T2SL where the cut-off wavelength can be tuned between any value from the MWIR to the VLWIR spectral regions. The main requirement is a good lattice match to the GaSb substrate. In this work, we have focused on barrier device architectures based on InAs/GaSb T2SLs, which absorb more strongly than gallium free InAs/InAsSb T2SLs, particularly in the LWIR spectral region. For XB*n* devices, we have demonstrated an operating temperature of ~125K and a QE of ~23%. Due to the small ratio of the valence mini-band width to the minority carrier energy fluctuation arising from disorder (e.g. layer width fluctuations), the transport is non-metallic, even when the T2SL period is reduced to 9 ML. A hole mobility of 31 cm^2/Vs was estimated from QE and dark current data, and was shown to be comparable to values deduced from similar data, recently reported by other workers for gallium free T2SLs. It was shown that such low mobility values correspond to hopping transport between localized states. The *n*-type T2SL minority carrier lifetime was 22 ns, corresponding to a diffusion length of ~0.6-0.8µm at 110K. In contrast, the diffusion length in the *p*-type T2SLs is an order of magnitude larger even though they exhibit an even shorter lifetime of 7.5 ns. The larger diffusion length is attributed to metallic minority electron transport, with an estimated mobility of 8,800 cm^2/Vs. As a result, the QE is much larger in XB*p* detectors, where we have observed a value of QE~64% in two pass test devices. In both cases, the short lifetimes are attributed to strong SRH recombination, and we suggest that traps in the GaSb layers with donor (acceptor) like character might account for both the short lifetimes and apparent suppression of Auger processes in XB*p* (XB*n*) devices. Passivation of such traps might thus lead to longer lifetimes and enhanced performance. Nevertheless, our Pelican D-LW FPA with a cut-off of ~9.3 µm exhibits an average detector QE of ~50% and background limited performance up to 90K, combined with good calibration stability and high spatial uniformity. This already makes the XB*p* T2SL technology an attractive alternative to MCT photodiode arrays, and it will be exploited in the future in further SCD products operating at other cut-off wavelengths.

ACKNOWLEDGEMENTS

The authors acknowledge technical support from Mr. S. Greenberg and Mr. Y Sandik, who were responsible for the smooth operation of the MBE machines, and Ms. H Schanzer, Mr. Hanan Geva, Ms. H. Moshe, Mr. Y. Caracenti, Ms. N. Hazan, Mr. I. Bogoslavski, Mr. Y. Osmo, Ms. L Krivolapov, and Ms. M. Menahem who have all contributed to the successful processing, packaging or characterization of the materials and devices.

REFERENCES

[1] Donald A. Reago, "*Future Army applications for IR focal plane arrays"*, Keynote address, Infrared Technology and Applications XXXIV Conference, Orlando, 2008. See http://spie.org/x20227.xml (2008)

[2] I. Shtrichman, D. Aronov, M. ben Ezra, I. Barkai, E. Berkowicz, M. Brumer, R. Fraenkel, A. Glozman, S. Grossman, E. Jacobsohn, O. Klin, P.C. Klipstein, I. Lukomsky, L. Shkedy, N. Snapi, M. Yassen, E. Weiss, "*High operating temperature epi-InSb and XBn-InAsSb photodetectors*", Proc. SPIE **8353**, 8353-2Y (2012)

[3] W.E. Tennant, *"Rule 07 Revisited: Still a Good Heuristic Predictor of p/n HgCdTe Photodiode Performance?"* Journal of Electronic Materials **39**, 1030 (2010)

[4] Y. Reibel, T. Augey, S. Verdet, P. Maillart, L. Rubaldo, D. Billon-Lanfrey, "*High Performance and Long-Range Cooled IR technologies in France*" Proc. SPIE **8704**, 8704-0B (2013)

[5] D. Lee, P. Drieske, J. Ellsworth, R. Cottier, A. Chen, S. Tallarico, A. Yulius, M. Carmody, E. Piquette, M. Zandian and S. Douglas, "*Law 19 - the ultimate photodiode performance metric*", Proc. 2019 U.S. Workshop on the Physics and Chemistry of II-VI materials" Conference workbook, pp13 -15, (2019)

[6] P.C. Klipstein (2003) "*Depletionless Photodiode with Suppressed Dark Current…*", US Patent 7,795,640 (2 July 2003)

[7] P.C. Klipstein (2006) "*Unipolar semiconductor photodetector with Suppressed Dark Current…*", US Patent 8,004,012 (6 April 2006)

[8] P.C. Klipstein, "*Semiconductor barrier photo-detector*" US Patent 9,627,563 (22 April 2013)

[9] P.C. Klipstein (2008) *"XBn Barrier Photodetectors for High Sensitivity and High Operating Temperature Infrared Sensors*", Proc. SPIE **6940**, 6940-2U

[10] P.C. Klipstein, Y. Gross, D. Aronov, M. Ben Ezra, E. Berkowicz, Y. Cohen, R. Fraenkel, A. Glozman, S. Grossman, O. Klin, I. Lukomsky, T. Marlowitz, L. Shkedy, I. Shtrichman, N. Snapi, A. Tuito, M. Yassen, and E. Weiss, "*Low SWaP MWIR detector based on XBn focal plane array"* Proc. SPIE **8704**, 8704-1S (2013)

[11] Y. Livneh, PC Klipstein, O Klin, N Snapi, S Grossman, A Glozman, and E Weiss, *Phys. Rev. B.* **86**, 235311 (2012); ibid, "Erratum", *Phys. Rev. B.* **90**, 039903 (2014)

[12] P.C. Klipstein, Y. Livneh, A. Glozman, S. Grossman, O. Klin, N. Snapi, and E. Weiss, "*k· p model for the energy dispersions and absorption spectra of InAs/GaSb type-II* superlattices," Journ. Electron. Mater. **43**, 2984 (2014)

[13] P.C. Klipstein, Y. Benny, S. Gliksman, A. Glozman, E. Hojman, O. Klin, L. Langof, I. Lukomsky, I. Marderfeld, M. Nitzani, N. Snapi, and E. Weiss, "*Minority carrier lifetime and diffusion length in type II superlattice barrier devices*", *Infrared. Phys. & Tech.* **96**, 155 (2019)

[14] N.F. Mott "*Metal-Insulator transitions*", Chapter 1, section 1.7, pp. 30-40, 1st Edition, Taylor and Francis: London (1974)

[15] P.C. Klipstein, O. Klin, S. Grossman, N. Snapi, I. Lukomsky, D. Aronov, M. Yassen, A. Glozman, T. Fishman, E. Berkowicz, O. Magen, I. Shtrichman, and E. Weiss, "*XBn barrier photodetectors based on InAsSb with high operating temperatures*", Optical Engineering **50**, 061002 (2011)

[16] Y.P. Varshni, "*Temperature dependence of the energy gap in semiconductors*", Physica **34**, 149 (1967)

[17] D. Donetsky, G. Belenky, S. P. Svensson, and S. Suchalkin, "*Minority carrier lifetime in type-2 InAs–GaSb strained-layer superlattices and bulk HgCdTe materials*", Appl. Phys. Lett. **97**, 052108 (2010)

[18] A.F. Ioffe and A.R. Regel, "*Non-crystalline, amorphous and liquid electronic semiconductors*", Progress in Semiconductors, **4**, 237 (1960)

[19] B.V. Olson, J. F. Klem, E.A. kadlec, J. K. Kim, M. D. Goldflam, S.D Hawkins, A. Tauke-Pedretti, W. T. Coon, T. R. Fortune, E. A. Shaner, and M.E. Flatté, "*Vertical hole transport and carrier localization in InAs/InAs$_{1-x}$Sb$_x$ Type II superlattice heterojunction bipolar transistors*", Phys. Rev. Applied **7**, 024016 (2017)

[20] F. Bertazzi, A. Tibaldi, M. Goano, J. A. Gonzalez Montoya, and E. Bellotti, "*Nonequilibrium Green's function modeling of type-II superlattice detectors and its connection to semiclassical approaches*", Phys. Rev. Appl. **14**, 014083 (2020)

[21] A. Soibel, D.Z. Ting, A.M Fisher, A. Khoshakhlagh, B. Pepper and S.D. Gunapala, "*Temperature dependence of diffusion length and mobility in mid-wavelength InAs/InAsSb superlattice infrared detectors*", Appl. Phys. Lett. **117**, 231103 (2020)

[22] G. Ariyawansa, J. Duran, C. Reyner and J. Scheihing, "*InAs/InAsSb strained layer superlattice mid-wavelength infrared detector for high temperature operation*", Micromachines **10**, 806 (2019)

[23] E.A. Kadlec, B.V. Olson, M.D. Goldflam, J.K. Kim, J. F. Klem, S.D. Hawkins, W.D. Coon, M.A. Cavaliere, A. Tauke-Pedretti, T.R. Fortune, C. T. harris and E.A. Shaner, "*Effects of electron doping level on minority carrier lifetimes in n-type mid-wave infrared InAs/InAs$_{1-x}$Sb$_x$ type II superlattices*", Appl. Phys. Lett. **109**, 261105 (2016)

[24] P.C. Klipstein, E. Avnon, D. Azulai, Y. Benny, R. Fraenkel, A. Glozman, E. Hojman, O. Klin, L. Krasovitsky, L. Langof, I. Lukomsky, M. Nitzani, I. Shtrichman, N. Rappaport, N. Snapi, E. Weiss, and A Tuito, "*Type II superlattice technology for LWIR detectors" Proc. SPIE* **9819**, 9819-0T (2016)

[25] P.C. Klipstein, E. Avnon, Y. Benny, R. Fraenkel, A. Glozman, S. Grossman, O. Klin, L. Langoff, Y. Livneh, I. Lukomsky, M. Nitzani, L. Shkedy, I. Shtrichman, N. Snapi, A. Tuito, and E. Weiss, "*InAs/GaSb type II superlattice barrier devices with a low dark current and a high-quantum efficiency*", *Proc. SPIE* **9070**, 9070-0U (2014)

[26] P.C. Klipstein, Y. Benny, Y. Cohen, N. Fraenkel, S. Gliksman, A. Glozman, I. Hirsh, L. Langof, I. Lukomsky, I. Marderfeld, B. Milgrom, M. Nitzani, D. Rakhmilevich, L. Shkedy, N. Snapi, I. Shtrichman, E. Weiss and N. Yaron, "*Performance limits of III-V barrier detectors*", Journal of Electronic Materials 49, 6893 (2020)

[27] S.Bandara, P.Maloney, N. Baril, J. Pellegrino, and M. Tidrow, (2011), "*Doping dependence of minority carrier lifetime in long-wave Sb-based type II superlattice infrared detector materials*", Optical Eng. **50**, 061015 (2011)

[28] C.H. Grein, J. Garland and M.E. Flatté , "*Strained and Unstrained Layer Superlattices for Infrared Detection*", Journ. Electron. Mater. **38**, 1800 (2009)